

Molecular Simulation of Structure and Diffusion at Smectite–Water Interfaces: Using Expanded Clay Interlayers as Model Nanopores

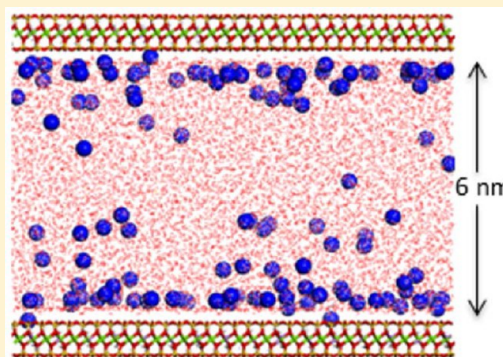
Jeffery A. Greathouse,^{*,†} David B. Hart,[†] Geoffrey M. Bowers,[‡] R. James Kirkpatrick,[§] and Randall T. Cygan[†]

[†]Sandia National Laboratories, Albuquerque, New Mexico 87185-0754, United States

[‡]Division of Chemistry, Alfred University, Alfred, New York 14802, United States

[§]College of Natural Science, Michigan State University, East Lansing, Michigan 48824, United States

ABSTRACT: In geologic settings relevant to a number of extraction and potential sequestration processes, nanopores bounded by clay mineral surfaces play a critical role in the transport of aqueous species. Solution structure and dynamics at clay–water interfaces are quite different from their bulk values, and the spatial extent of this disruption remains a topic of current interest. We have used molecular dynamics simulations to investigate the structure and diffusion of aqueous solutions in clay nanopores approximately 6 nm thick, comparing the effect of clay composition with model Na-hectorite and Na-montmorillonite surfaces. In addition to structural properties at the interface, water and ion diffusion coefficients were calculated within each aqueous layer at the interface, as well as in the central bulk-like region of the nanopore. The results show similar solution structure and diffusion properties at each surface, with subtle differences in sodium adsorption complexes and water structure in the first adsorbed layer due to different arrangements of layer hydroxyl groups in the two clay models. Interestingly, the extent of surface disruption on bulk-like solution structure and diffusion extends to only a few water layers. A comparison of sodium ion residence times confirms similar behavior of inner-sphere and outer-sphere surface complexes at each clay surface, but ~1% of sodium ions adsorb in ditrigonal cavities on the hectorite surface. The presence of these anhydrous ions is consistent with highly immobile anhydrous ions seen in previous nuclear magnetic resonance spectroscopic measurements of hectorite pastes.



INTRODUCTION

Chemical reactivity and transport of water and aqueous species in nanoporous materials are typically controlled by structure, composition, charge distribution, protonation state, and related properties of the mineral–water interfaces. Surface chemistry and the reactivity of clay minerals, in particular, can influence mineral–water interfaces and control many geochemical processes in the environment.^{1,2} These include adsorption, dissolution, precipitation, solute and water diffusion, nucleation, and growth phenomena that can impact mesoscopic and macroscopic rock properties, such as permeability, porosity, wettability, and mechanical strength.

Recent interest in the extraction of gas and oil from unconventional geological reservoirs such as shale rocks^{3–5} highlights the need for an improved assessment of nanoporosity and the physical chemistry of the dominant clay–water interactions in such tight rock environments. Similarly, the interfacial chemistry of clay–water nanopores is relevant to understanding the geochemistry of CO₂ storage and sequestration in the subsurface,^{6–9} in performance assessment activities for safe nuclear waste treatment and storage in geological formations,^{10–13} in evaluating reactive transport and flow in soils and sediments,^{14–17} and in other related environmental and geological applications.^{18–20}

Molecular details of these geochemical processes are typically beyond the sensitivity of most experimental and analytical techniques and therefore require accurate models and simulation methods to guide the interpretation of the molecular behavior. Molecular simulations provide a unique probe of the mineral–water interface and offer details of the structure, energetics, and dynamics of the interface, including the mineral substrate and adsorbates, solutes, and water molecules of the aqueous phase. Molecular dynamics (MD) simulations offer analysis of time-dependent processes ranging from femto- to pico- to nanoseconds and for spatial scales from Ångströms to tens of nanometers. In some instances these molecular results can influence the interpretation of geological events involving large scales of time (millennia to millions of years) and space (meters to kilometers), although such upscaling approaches remain a challenge for many geological applications.^{21–24}

Of the spectroscopic methods that are complementary to molecular simulation, nuclear magnetic resonance (NMR) spectroscopy can be used to probe interlayer dynamics at time scales accessible to MD simulation.^{25–32} Hectorite is a swelling

Received: April 6, 2015

Revised: June 23, 2015

Published: July 20, 2015

(smectite) clay with layer charge localized in the octahedral sheet that results from Li^+ substitution for Mg^{2+} . The limited amount of Fe that occurs in natural hectorite clays makes it an ideal material to experimentally probe the structure and dynamics of water and interlayer ions in the clay mineral using NMR. The low Fe content enables NMR spectroscopists to avoid the line broadening and related interferences associated with paramagnetic centers of Fe that typically occur in the common montmorillonite form of smectite in which Al, Mg, and Fe reside in the octahedral sheet. NMR-based studies of hectorite have established constraints on the rates of water dynamics, including reorientation and librational behavior, provided insight into the activation energies of dynamic processes, and suggested models for the geometry and mechanism of H_2O dynamics over a range of temperature scales. Similar insights to the rate and mechanism of cation motion have been provided for cations that interact with the interlayer and external clay surfaces, such as at the ditrigonal cavity site.^{26–28,33,34} These spectroscopic findings involving detailed molecular mechanisms of the interlayer dynamics were subsequently supported by the recent MD simulations of Na-hectorite interlayers.³⁵ Neutron scattering methods and complementary MD simulations have also been used to examine the dynamics of interlayer water in hectorite and suggest slower rates and greater activation energies for diffusion of water molecules parallel to the clay surface.^{36–39}

Numerous studies have examined the diffusion of water and various chemical species in clay mineral interlayers using MD simulation.^{35–46} Most of these investigations have derived diffusion coefficients of interlayer water and alkali cations (Na^+ , Cs^+ , etc.), often at multiple hydration states, which typically for smectite clays can occur as stable one-, two-, or three-layer hydrates. In general, diffusion rates for cations and water increase with interlayer water content, but these rates also depend on cation charge, cation hydration energy, clay surface structure, and clay charge distribution. Several recent molecular simulation studies have investigated diffusion rates of cations or water molecules, or their distribution, on external surfaces of clay and related minerals. These efforts have explored the wetting process through simulations of the sequential hydration with water monolayers to, in some cases, a water-saturated nanopore: brucite ($\text{Mg}(\text{OH})_2$),⁴⁷ boehmite ($\gamma\text{-AlO}(\text{OH})$),⁴⁸ muscovite ($\text{KAl}_2(\text{Si}_3\text{Al})\text{O}_{10}(\text{OH})_2$),⁴⁹ montmorillonite,^{24,46,50–52} and other layered minerals.⁵³

In the present computational study, we extend the previous MD studies of hectorite^{35–37,45,54} by examining the structure and behavior of water and Na^+ on the external basal surface of hectorite. Rather than examine the confinement of cations and water within the interlayer, our simulations represent the water-saturated environment expected for a nanopore in which the distribution of water and Na^+ in an aqueous pore is impacted by two opposing hectorite surfaces. MD simulations of an equivalent nanopore based on montmorillonite surfaces are used to compare the influence of substrate structure and charge distribution on the aqueous structure of the nanopore. Of particular note, our analysis of water and Na^+ diffusion in the nanopores is based on survival probabilities in well-defined water layers. The resulting profile of diffusion coefficients clearly shows the effect of surface properties on diffusion in clay nanopores.

SIMULATION METHODS

Montmorillonite and hectorite were investigated as model smectite minerals to represent the surfaces exposed in a clay-bounded nanopore. Basal surfaces of smectite phyllosilicates typically dominate the total surface area of these phases, although edge surfaces can represent the more reactive surface sites for clay minerals. While clay nanopores could contain hydroxylated edge surfaces, we limit the present study to basal surfaces for consistency with previous MD studies of hectorite interlayers.^{35–37} Additionally, our nanopore model is analogous to the hectorite paste samples used in recent NMR experiments, where the total water content is known to be well into the osmotic swelling regime [interlayer spacing ~ 3 water layers (0.75 nm) and greater].²⁷ The initial dry hectorite model was built from an orthogonalized unit cell with an anhydrous stoichiometry of $\text{M}_{0.5}(\text{Mg}_{2.5}\text{Li}_{0.5})\text{Si}_4\text{O}_{10}(\text{OH})_2$ and dimensions of $x = 5.25 \text{ \AA}$, $y = 9.21 \text{ \AA}$, and $z = 9.35 \text{ \AA}$, where M represents the charge-compensating interlayer cation. The initial dry montmorillonite model was derived from a unit cell of $\text{M}_{0.5}(\text{Al}_{1.5}\text{Mg}_{0.5})\text{Si}_4\text{O}_{10}(\text{OH})_2$ with dimensions of $x = 5.17 \text{ \AA}$, $y = 9.01 \text{ \AA}$, and $z = 9.31 \text{ \AA}$. Layer charge for each model was localized in the octahedral sheet and is associated with the heterovalent substitution of metal cations; that is, Li^+ substitution for Mg^{2+} in hectorite and Mg^{2+} substitution for Al^{3+} in montmorillonite. Additionally, hectorite has all three available octahedral sites occupied (trioctahedral smectite) whereas montmorillonite has one vacant site for every two occupied octahedral sites (dioctahedral smectite). The extent of octahedral substitution determines the total layer charge and influences the cation exchange capacity and swelling property of the clay mineral. Both molecular models possess a layer charge of $-0.5 e$ per $\text{O}_{10}(\text{OH})_2$, a charge representative of a swelling smectite phase.

Each model was expanded to a $16 \times 8 \times 4$ supercell with full periodic boundaries and having four interlayer regions. Neutral charge was maintained by adding 128 Na^+ per interlayer. Three of the interlayers were kept dry, including the layer through which the z periodic boundary passed. The remaining interlayer was expanded with 10 240 H_2O molecules to form a nanopore. The final dimensions of the supercell for hectorite were $x = 84.0 \text{ \AA}$, $y = 73.7 \text{ \AA}$, and $z = 89.9 \text{ \AA}$, with a total of 52 736 atoms. The final dimensions of the montmorillonite supercell were $x = 83.0 \text{ \AA}$, $y = 72.1 \text{ \AA}$, and $z = 88.4 \text{ \AA}$, with 51 712 total atoms. A snapshot of an MD-equilibrated hectorite nanopore is shown in Figure 1.

Force field parameters were taken from Clayff and assigned to each atom of the two clay models.⁵⁵ This fully flexible force field has been successfully applied to many oxide, hydroxide, and clay mineral systems of environmental interest.^{35,36,40,47–49,53,56–69} Clayff consists almost exclusively of nonbonded (van der Waals and electrostatic) energy terms, with bonded interactions only defined for layer hydroxyl groups and water molecules. Force field parameters were taken from Clayff without modification except atomic charges of the *obss* (bridging oxygen with double substitution) and *obos* (bridging oxygen with single substitution) atomic charges, which were adjusted to maintain electroneutrality. The revised atomic charges are -1.237725 (*obss* in hectorite) and -1.180850 (*obos* in montmorillonite).

All MD simulations were performed with three-dimensional periodic boundary conditions using the LAMMPS software.⁷⁰ A real-space cutoff of 10.0 \AA was used for short-range interactions,

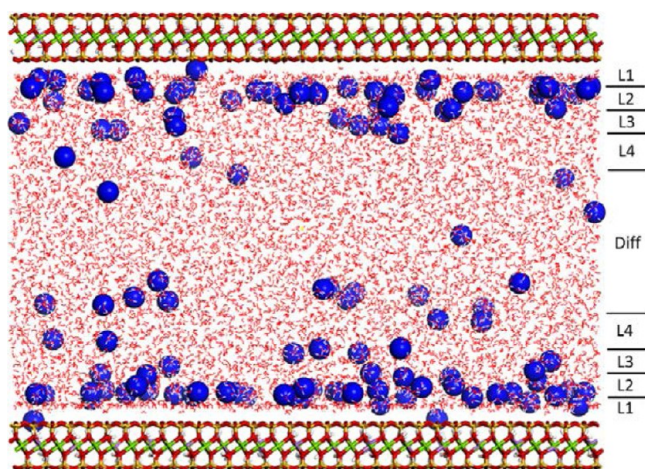


Figure 1. Snapshot of the hectorite simulation supercell representing the equilibrated nanopore structure. Atoms are colored as follows: Na (blue), O (red), H (white), Si (yellow), Li (purple), and Mg (green). Aqueous layers are identified as L1 – L4 and Diff (diffuse).

and long-range electrostatics were calculated with the particle–particle particle–mesh (PPPM) summation algorithm⁷¹ at a precision of 1.0×10^{-4} . A time step of 1 fs was used for long-range interactions, and short-range interactions were calculated every 0.5 fs. During all simulations, one atom in each clay layer was “pinned”, that is, excluded from thermodynamic calculations to prevent unwanted movements of the clay layers. Such translational moves are a consequence of random initial velocities and can lead to a shearing motion between clay layers. The four pinned atoms were selected from the Mg atoms of the octahedral sheet for hectorite and from the Al atoms of the octahedral sheet for montmorillonite. A minimum of one atom in each clay layer is needed to prevent translation, but a total of four atoms is necessary to avoid potential rotations and realignment of the layers, which would significantly complicate the trajectory analysis.

The simulation methodology is summarized in Table 1 and is similar to our previous MD simulation studies.^{72–74} Where

Table 1. Summary of MD Simulation Methodology

ensemble	mobile atoms	temperature (K)	run time (ns)
from initial supercell configurations			
NVE	all but pinned atoms	298	0.05
NVT		298	0.05
NPT		298	1.0
NVT	water and Na ⁺ only	1000	0.2
from each new configuration output			
NVT	all but pinned atoms	1000 → 298	0.1
NVT		298.0	5.0
NVT		298.0	5.0

appropriate, Nosé–Hoover thermostats and barostats were used as implemented in LAMMPS with relaxation times of 0.1 and 1.5 ps, respectively. The initial configuration was equilibrated with a 50 ps NVE (number of particles N , volume V , and potential energy E) simulation at a temperature of 298.0 K to allow atoms to relax from the initial lattice configuration. This was followed by a 50 ps NVT (temperature T) simulation. The supercell thickness was then equilibrated by a 1 ns NPT (pressure P set to 0 bar) simulation. Only the supercell z -dimension was allowed to change during the NPT simulation

(note that pinned atoms are fixed in scaled coordinates only, allowing their real coordinates to change as cell parameters changed). Each of the equilibrated supercells was then used to create ten initial configurations. All atoms were held fixed except for sodium ions and water molecules, which were assigned random initial velocities for a 200 ps NVT simulation at 1000 K. These short simulations resulted in random sodium configurations throughout each nanopore, removing any configurational bias from the previous NPT simulation at 298 K. Configurations were saved every 10 ps during the final 100 ps of simulation, providing ten random initial configurations for each nanopore model.

Each random configuration was cooled to 298.0 K, followed by a 10 ns NVT simulation in which all atoms moved except the four originally pinned atoms. Structural properties were obtained from simulation trajectories over the final 5 ns with a sampling frequency of 200 fs. A total of 50 ns of trajectory data were collected for each nanopore model.

Nanopore Structure. One-dimensional (1D) atomic density profiles were obtained from MD trajectories and averaged over the ten replicate simulations. Water layers were defined by identifying minima in the water oxygen (O_w) density profiles. The average position of siloxane oxygen atoms at the lower clay–solution interface (Figure 1) was set to $z = 0.0$ to provide a consistent point of reference. The percentage of sodium ions corresponding to each peak in the 1D density profile was obtained from integration and averaged over both surfaces in each replicate simulation. Representative two-dimensional (2D) density profiles were obtained from a single MD trajectory for each model nanopore.

Diffusion Coefficients. Following Liu et al.,⁷⁵ we applied virtual boundary conditions during the analysis to calculate diffusion coefficients for water (O_w atoms) and sodium ions in specified layers in the nanopores. Thus, O_w and Na⁺ contribute to the mean-square displacement (MSD) for a given layer only when present in that layer. The relative time step of an atom’s contribution to the MSD is reset to time $t = 0$ each time that species enters the layer. We define $S(t, t + \tau)$ as the set of all $N(t, t + \tau)$ particles that stay within a layer between time t and $t + \tau$, where $N(t)$ is the number of particles in the layer at time t . Using atomic positions in the x -direction for atoms in layer L1 as an example, the MSD is calculated as

$$\langle \Delta x^2(\tau) \rangle_{L1} = \frac{1}{T_{\max}} \sum_{t=1}^{T_{\max}} \frac{1}{N(t)} \sum_{i \in S(t, t+\tau)} (x_i(t+\tau) - x_i(t))^2 \quad (1)$$

The survival probability $P(t)$ that a particle is still within layer L1 is

$$P(\tau)_{L1} = \frac{1}{T_{\max}} \sum_{t=1}^{T_{\max}} \frac{N(t, t+\tau)}{N(t)} \quad (2)$$

where T_{\max} is the total number of steps in the time window of length τ , ranging from Δt to $M\Delta t$, where M is the maximum number of lags. The expression for D_{xx} and D_{yy} can be written as

$$D_{xx, L1} = \lim_{\tau \rightarrow \infty} \frac{\langle \Delta x^2(\tau) \rangle_j}{2\tau P(\tau)} \quad (3)$$

In practice, however, the limit is undefined for large τ when calculated for a bounded layer. As τ increases, the MSD increases over short displacements before decreasing as the

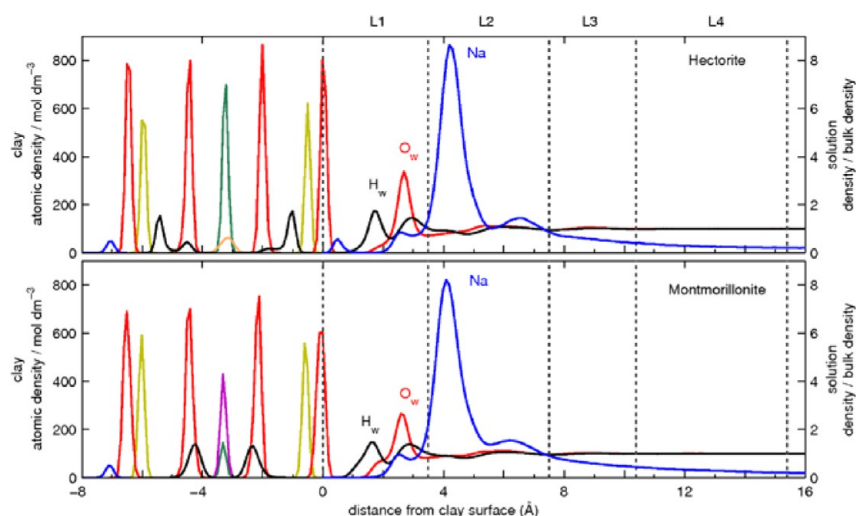


Figure 2. 1D atomic density profiles in hectorite and montmorillonite nanopores relative to surface oxygen atoms. Aqueous regions are labeled along the top horizontal axis as L1, L2, L3, and L4, with boundaries between these layers indicated by gray dotted lines. Density units are shown separately for clay atoms (left axis) and solution atoms (right axis). Only one of the four clay layers is shown in each of the atomic profiles. Colors are as follows: Na (blue), O (red), H (black), Si (brown), Mg (green), Li (orange), and Al (purple).

number of surviving particles approaches zero. The survival probability vanishes at the same rate as the MSD, leading to the numerical instability inherent in eq 3. After some trial and error, we chose the following rule, as it allows consistent application without requiring individual determination of window sizes. The diffusion coefficient in each direction parallel to the surface (D_{xx} or D_{yy}) is calculated directly as

$$D_{xx,L1} = \frac{\langle \Delta x^2(\tau_m) \rangle_{L1}}{2\tau_m P(\tau_m)} \quad (4)$$

where τ_m corresponds to the maximum in the MSD for a given species in a given layer. For the results presented here, the diffusion coefficients D_{xx} and D_{yy} were averaged together to obtain D_{\parallel} (diffusion coefficient parallel to the surface). It should be noted that for “thin” regions—in this case <5 Å in width—the maximum MSD(t) typically occurred when $P(t)$ was between 0.3 and 0.4. The value of τ_m was similar to the calculated average residence time.

Residence Times. Noting that particle transport between aqueous layers near a surface is similar to diffusion from a thin film, the time dependence of particle survival probability in a layer was fit with an exponential decay constant γ

$$P(t) = P_0 e^{-\gamma t} \quad (5)$$

where the characteristic residence time $T_R = 1/\gamma$.

Residence times and diffusion coefficients were calculated for each replicate simulation and surface individually and then averaged together as $n = 20$ samples for each nanopore. While diffusion coefficients perpendicular to the surface could be calculated with a multiple regression model, this was not done in the present study because we are interested in diffusion through nanopores.

RESULTS AND DISCUSSION

The average interfacial structure at the lower nanopore surface of each clay mineral is shown in Figure 2. Results for the upper surfaces are equivalent but are not shown for clarity. Different atomic densities in the clay and aqueous regions were used for ease of viewing, so some peaks in the clay layers appear small

compared to those in the aqueous region (e.g., Na). As expected, density peaks corresponding to hectorite and montmorillonite layers are nearly identical, except for the distribution of hydroxyl hydrogen atoms. The lack of vacancy sites in the octahedral sheet of trioctahedral hectorite forces most of the hydroxyl groups to be oriented perpendicular to the sheets (large H peaks at -5.4 and -1.0 Å) with the hydroxyl groups centered in the ditrigonal cavity.⁷⁶ However, some sodium ions adsorb in ditrigonal cavities on the hectorite surface (Na^+ peak at 0.5 Å), which directs those hydroxyl groups into a more parallel orientation (small H peaks at -1.8 and -4.5 Å).

The asymmetry observed in the hydrogen peaks associated with the hectorite hydroxyl groups is due to the aqueous phase in contact with only one of the two hectorite surfaces (>0 Å). The hectorite surface at -6.5 Å is adjacent to a dry interlayer region consisting only of sodium ions that remain adsorbed in ditrigonal cavities (-7.0 Å). The orientation of layer hydroxyl groups parallel (perpendicular) to the clay sheets is governed by the presence (absence) of a sodium ion in that ditrigonal cavity, respectively. Previous simulations of the neutral end member of this clay mineral (talca) indicate that all layer hydroxyl groups are oriented perpendicular to the basal surface.⁷⁷ In contrast, montmorillonite layers contain octahedral vacancy sites that allow for layer hydroxyl groups to be oriented nearly parallel to the clay sheets (broad H peaks at -2.3 and -4.2 Å).

Although MD snapshots were not stored frequently enough to conclusively determine the formation mechanism of anhydrous sodium ions on the hectorite surface, we believe that the approach of the ion into the ditrigonal cavity causes the proximate layer hydroxyl group to tilt away due to repulsion. Anhydrous sodium ions are present in the dry interlayers of hectorite and also on the hydrated hectorite surface, near an octahedral lithium ion (charge site). Additionally, the layer hydroxyl group always tilts toward the lithium site rather than a magnesium site, presumably because the lithium site results in reduced electrostatic repulsion compared to a magnesium site. The favorable interaction between these anhydrous sodium ions and the six oxygen atoms lining the ditrigonal cavity

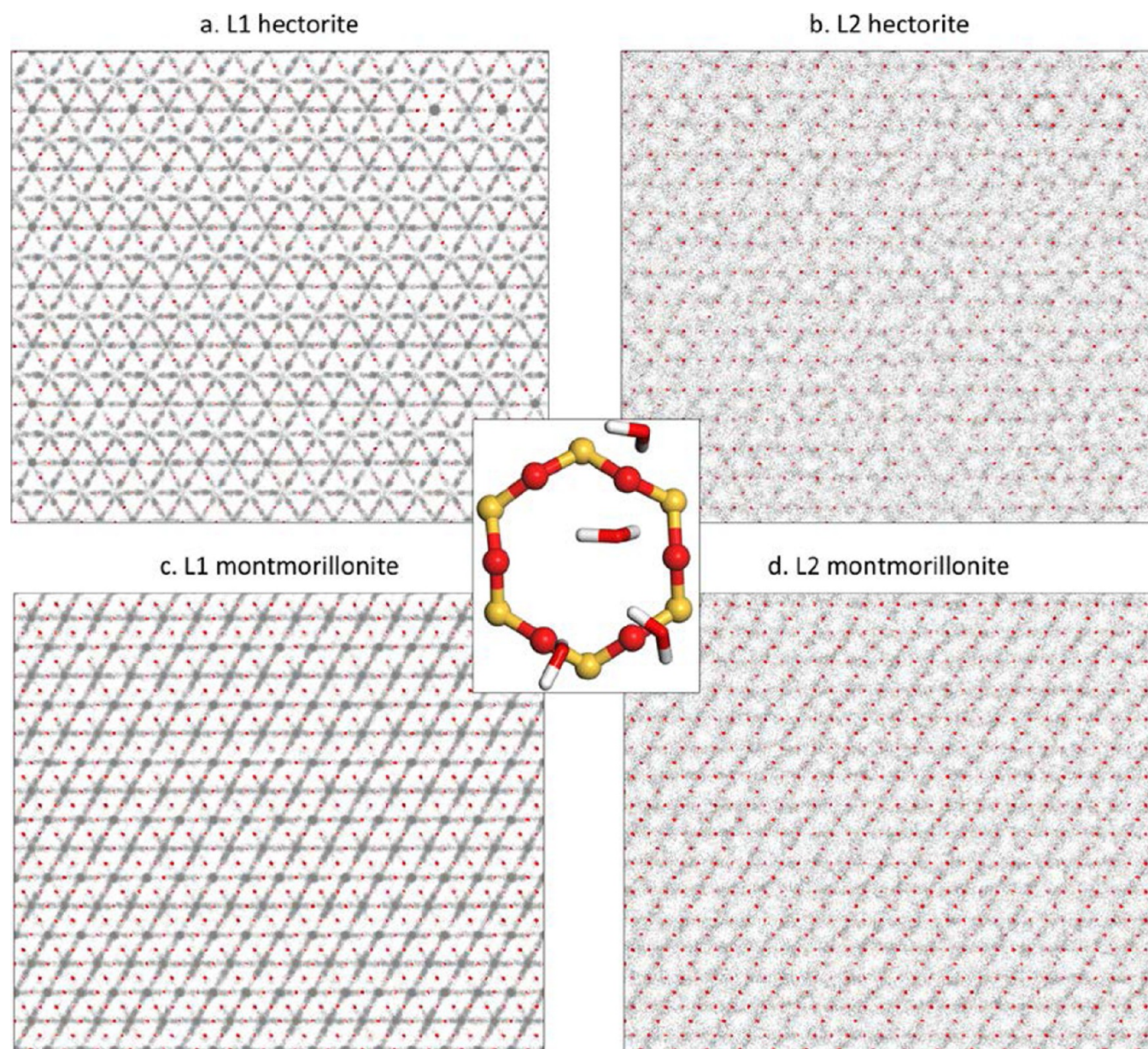


Figure 3. Two-dimensional atomic density profiles (xy plane) for (a, b) hectorite and (c, d) montmorillonite showing the location of water oxygen atoms in the first and second adsorption layers (gray) overlaid on surface oxygen sites (red). The inset (middle) shows one siloxane ring and adsorbed L1 water molecules.

appears to overcome the electrostatic and steric repulsion between the hydroxyl hydrogen atom and the octahedral lithium ion. Differences in interfacial structure between these two similar mineral surfaces are likely governed by the presence of vacancy sites in montmorillonite, but detailed quantum mechanical calculations would be needed to provide further explanation.

In the aqueous pores, the distributions of water molecules and sodium ions beyond 2.0 Å from the hectorite and montmorillonite surfaces are nearly identical. In Figure 2, distinct aqueous layers relevant to both clay surfaces are defined as L1, L2, and L3 based on minima in the water density profiles. For montmorillonite, the first peak in the water hydrogen (H_w) profile is slightly broader near the surface compared to the corresponding hectorite peak, and the water oxygen (O_w) peak has a small shoulder between 1.5 and 2.0 Å that is absent near the hectorite surface. Layers farther from the clay mineral

surface are less ordered than the first three layers, so an arbitrary layer thickness of 5.0 Å was used to define layer L4. All water molecules beyond L4 are termed “diffuse.”

Small differences in aqueous structure very near the surfaces greatly affect the 2D arrangement of these adsorbed layers (Figures 3 and 4). The 1D water profiles indicate a more ordered water structure at the hectorite surface, and this results in substantially more 2D ordering compared to the montmorillonite surface (Figure 3a, c). For water molecules adsorbed on the hectorite surface (L1 layer), Figure 3a indicates that O_w atoms form a 2D hexagonal structure based on the strong interactions between these L1 waters and surface oxygen atoms. In contrast, Figure 3c shows that L1 waters on the montmorillonite surface have primary adsorption sites above the ditrigonal cavities, with lines of reduced O_w density corresponding to water exchange between adsorption sites. Despite this noticeable difference in 2D structure, water

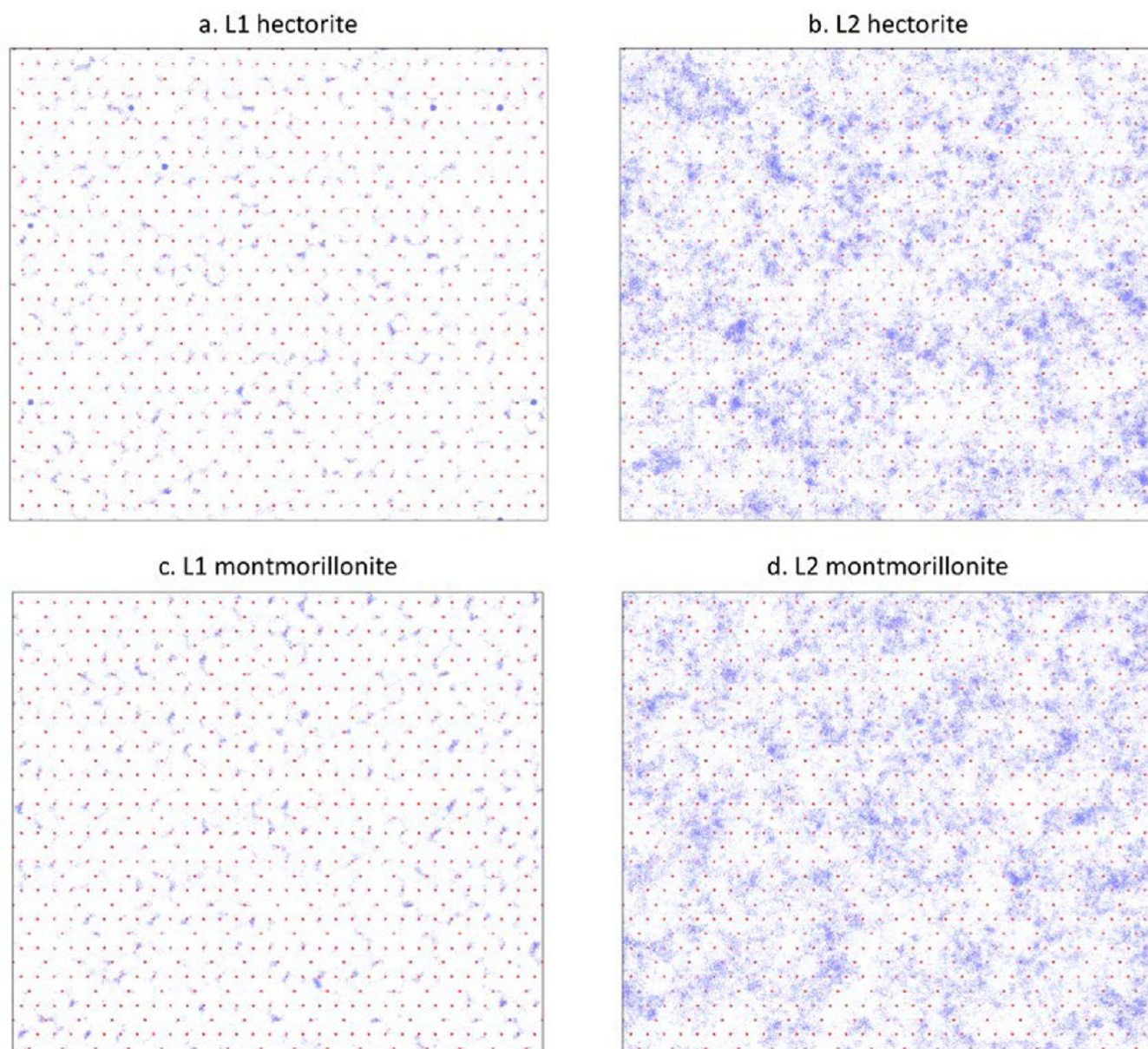


Figure 4. Two-dimensional atomic density profiles (xy plane) for (a, b) hectorite and (c, d) montmorillonite showing the location of sodium ions in the first and second adsorption layers (blue) overlaid on surface oxygen sites (red).

molecules in the L1 layers on both surfaces display nearly identical hydrogen bond coordination to neighboring water molecules and surface oxygen atoms. An analysis of radial distribution functions (data not shown) reveals that the average coordination number between H_w atoms and O_{surface} atoms is slightly greater for hectorite (0.58) than for montmorillonite (0.45 Å), which is compensated by a slightly smaller coordination number for intermolecular water ($O_w - H_w$) interactions at the hectorite surface.

There is substantially less 2D ordering of water in the L2 layers (Figure 3b, d), as predicted by the very broad L2 peaks in the 1D profiles (Figure 2). However, traces of ordered water in the L1 layer are still exhibited in the L2 layer, at distances of up to 7.5 Å from the surface. Comparing the L1 and L2 water profiles side-by-side, we observe that lines of high water density in the L2 layer are offset from the corresponding density lines in the L1 layers.

The 1D distribution of sodium ions near the clay mineral surfaces reveals two familiar adsorption complexes and one complex unique to the hectorite surface. In the 1D density profile (Figure 2), the Na^+ peak at 0.5 Å is due to ions adsorbed in the ditrigonal cavities on the hydrated hectorite surface. These adsorbed ions have been termed anhydrous, because their first hydration shells contain primarily surface oxygen atoms.²⁷ This adsorption site is not observed on the montmorillonite surface. The L1 layer at both clay mineral surfaces shows a minor sodium peak at 2.5 Å (Figure 2), corresponding to inner-sphere (IS) surface complexes. The vast majority of adsorbed ions exist as outer-sphere (OS) surface complexes represented by broad peaks ~ 4 Å from each surface (Figure 2). The relatively high sodium density between IS and OS peaks suggests rapid exchange between these sodium surface complexes.

The 2D distributions of sodium ions in the L1 layers (Figure 4a, c) show much less ordering than water molecules in the

same layer. Anhydrous ions appear as distinct blue dots above ditrigonal cavities on the hectorite surface (Figure 4a), and their surface locations correlate exactly with the unusual water distribution above those cavities (Figure 3a). The 2D traces of IS ions are aligned with surface oxygen atoms that are coordinated to these ions. There is no discernible 2D structure of OS ions on either surface (Figure 4b, d), because these ions are coordinated to the surface via weak water-surface hydrogen bonds rather than stronger ion-surface electrostatic interactions.

The gradual hydration of ions with increasing ion-surface distance is presented in Figure 5 with representative snapshots of each sodium surface complex. The coordination shell of anhydrous ions consists almost entirely of surface oxygen atoms

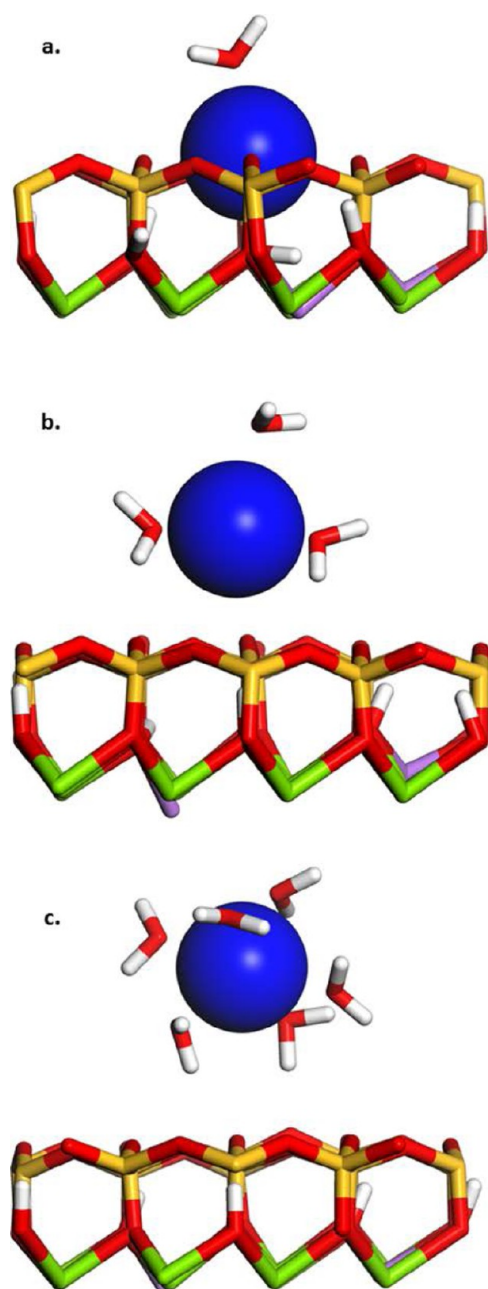


Figure 5. Representative snapshots (xz plane) showing adsorbed sodium ions in (a) anhydrous, (b) inner-sphere, and (c) outer-sphere surface complexes on the hectorite surface. Atoms are colored as in Figure 1.

(Figure 5a). One water molecule can coordinate directly above the ion, indicated by the small circular regions of high water density centered over some ditrigonal cavities on the hectorite surface (Figure 4a). On both surfaces, IS complexes are partially coordinated by surface oxygen atoms (Figure 5b), and OS complexes are completely hydrated (Figure 5c).

Sodium peaks in the 1D distribution were integrated to obtain the percent composition in each aqueous layer (Table 2). Residence times of ions and water molecules in each layer

Table 2. Percentage of Sodium Ions in Each Adsorption Layer in the Aqueous Pores

adsorption layer	hectorite	montmorillonite
anhydrous (L1)	0.9	
inner-sphere (L1)	3.3	3.9
outer-sphere (L2)	53.1	52.9
diffuse (L3 – L4)	42.6	43.3

were obtained from the diffusion analysis and are presented in Table 3. As shown in Table 2, these anhydrous ions account for

Table 3. Water and Sodium Ion Residence Times (ps)

species	adsorption layer	hectorite	montmorillonite
H ₂ O	L1	11.0(2)	13.5(6)
	L2	93.0(1)	90.1(1)
Na ⁺	anhydrous (L1)	65(22)	
	inner-sphere (L1)	2.3(1)	3.1(2)
	outer-sphere (L2)	31.1(5)	27.1(5)

only a small portion (1%) of the aqueous ion distribution on the hectorite surface. In fact, the anhydrous surface complex occurs so infrequently that its presence could easily be overlooked in simulations using smaller system sizes or shorter run times. The highly coordinated first shell about these ions consists of surface oxygen atoms, resulting in a long residence time (65 ps) for anhydrous ions.

Moving away from the surfaces, inner-sphere ions (L1 layer) constitute only a small fraction (3–4%) of sodium ions in the pores, and their 2D density profiles (Figure 4a, c) indicate limited surface diffusion paths. These ions have a relatively short residence time in the L1 layer (2–3 ps) before moving away from the surface and into the L2 layer. The similarity of IS ion properties between the hectorite and montmorillonite surfaces (density profiles, percent composition, and residence times) suggests that effects due to clay structural features (octahedral vacancy sites and orientation of layer hydroxyl groups) have little influence on the interfacial structure even at a short distance of 2.5 Å from the surface.

Outer-sphere ions (L2 layer) represent 53% of all aqueous ions and ~93% of adsorbed ions at each surface. Table 2 shows that the residence times of OS ions (~30 ps) are an order of magnitude longer than those of IS ions. For reference, a 30 ps residence time corresponds to 167 exchange events per ion (into or out of the L2 layer) during a 5 ns production simulation. The large model systems and long simulation times used in this study are critical to obtaining accurate statistics for analysis of ion residence times and aqueous diffusion. Finally, the partitioning of sodium ions between short-lived IS and long-lived OS complexes suggests that the latter are more energetically stable, although we have not attempted to calculate adsorption free energies. Several recent studies have

used potential of mean force calculations to derive these free energies for the adsorption of cations and molecules onto minerals and zeolite materials.^{78–80}

The trend for water residence times is similar to that for sodium ions: residence times for OS-hydrating (L2) and IS-hydrating (L1) waters are approximately 90 and 10 ps, respectively. The consistency between ion and water residence times in aqueous layers can be attributed to the ability of an ion to maintain a partial or full hydration shell while exchanging between adsorption layers. The residence time of water in the first coordination shell of a sodium ion is ~ 20 ps, calculated from MD simulations using a related water model at 298 K.^{81,82} Within each layer, the exchange of water molecules between ion hydration shells therefore results in longer residence times for water compared to sodium ions.

The mobility of water and ions in the nanopores is shown graphically as diffusion coefficients for each aqueous layer in Figure 6. Results are presented only for diffusion parallel to the

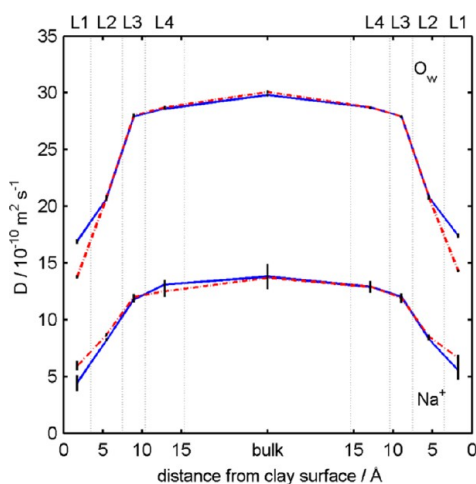


Figure 6. Diffusion coefficients for water molecules (O_w , top) and sodium ions (Na^+ , bottom) for each adsorption layer in Na-hectorite (blue) and Na-montmorillonite (red) nanopores, for translational motion parallel to the basal surfaces (xy plane). Boundaries between adsorption layers are indicated by gray dotted lines, and uncertainties for each diffusion coefficient are indicated by vertical lines.

basal surfaces (xy plane), because this motion best represents transport through such pores. Beyond the first aqueous layer (L1), diffusion is similar for each clay surface. Interestingly, both ion and water diffusion coefficients (D_w and D_{Na}) approach bulk-like values within 10 Å of the surface.

The water diffusion profiles are also consistent with 1D atomic density profiles of water near a variety of other mineral surfaces, which also show bulk-like structure within 10 Å of the surface regardless of surface composition, surface charge, or hydrophobicity.⁵³ For reference, D_w and D_{Na} values in the bulk layer are slightly less than values obtained from a simulated dilute solution (4 Na^+ and 4 Cl^- in a 50 Å cubic box) at 300 K using these same ion and water potentials: $D_w = 32.8 \times 10^{-10} \text{ m}^2 \cdot \text{s}^{-1}$ and $D_{Na} = 15.4 \times 10^{-10} \text{ m}^2 \cdot \text{s}^{-1}$. Translational motion normal to the clay surfaces was also analyzed, but Figure 6 indicates the presence of bulk-like diffusion coefficients within a few aqueous layers of the clay surfaces.

The water diffusion profiles presented here are qualitatively similar to those reported from MD simulations in much larger (10 nm),¹⁹ and slightly smaller (3.3 nm),^{46,83} montmorillonite

nanopores, in which the transition from surface-like to bulk-like water diffusion occurs between 1 and 2 nm from the surface in each case. It is worth noting that in our simulations D_w never reaches the bulk value for a roughly 6 nm pore, while in the 10 nm pore the bulk value is surpassed for water molecules >3 nm from the surface.¹⁹ This difference in water diffusion behavior could be due to the slightly different water models used (rigid SPC/E in the previous work compared with flexible SPC here), or possibly system size effects in the lateral dimensions. A recent comparison of the effect of simulation box size and shape on diffusion coefficients suggests that both properties can significantly affect fluid diffusion coefficients.⁸⁴

Although much more work is needed to make generalizations about the effect of nanopore thickness on diffusion, the results presented here and elsewhere indicate that bulk-like solution behavior is seen within 1–2 nm of strongly interacting clay surfaces.

Average values for D_w and D_{Na} are given in Table 4 for the L1 and L2 layers, where differences between hectorite and

Table 4. Lateral Diffusion Coefficients ($10^{-10} \text{ m}^2 \cdot \text{s}^{-1}$) in the First Two Water Layers

species	adsorption layer	hectorite	montmorillonite
H_2O	L1	17.2(3)	14.0(2)
	L2	20.7(2)	20.8(1)
Na^+	L1	5(1)	6(1)
	L2	8.3(1)	8.6(2)

montmorillonite surfaces are observed. In the L1 layer, D_w for hectorite is slightly greater than that of montmorillonite, consistent with the slightly shorter residence times at the hectorite surface (Table 3). Although the 2D density profiles indicate a more ordered water structure on the hectorite surface (Figure 3a, c), the regions of high water density near ditrigonal cavity sites on the montmorillonite surface result in slower lateral motion. In the L1 layer of hectorite, D_{Na} includes contributions from both anhydrous and inner-sphere sodium ions, with the latter showing very limited mobility due to the constrained coordination environment.

Diffusion coefficients in the second aqueous layer have not reached the bulk-like plateau values seen in Figure 6, but these values are nearly identical at the two surfaces. Note that the majority of ions in the L2 layer are adsorbed as outer-sphere surface complexes, but some ions farther from the surface form a shoulder at ~ 5 Å (Figure 2). These “diffuse” ions exhibit more rapid lateral motion, resulting in slightly increased D_{Na} values.

CONCLUSIONS

Molecular dynamics simulations of clay-based nanopores provide significant insight into the structure, dynamics, and interactions of water and Na^+ at clay mineral–solution interfaces. Through a comparison of two similar smectite minerals—hectorite and montmorillonite—with equivalent charge and comparable localized charge distribution, we observe subtle differences in the adsorption and diffusion behavior of water and Na^+ at the clay surface. Equilibrated structures for both hectorite and montmorillonite exhibit inner- and outer-sphere complexes for Na^+ adsorption at the siloxane surface of the clay tetrahedral sheets. However, the structure of trioctahedral hectorite has hydroxyl groups primarily directed toward the ditrigonal cavity, while the dioctahedral montmor-

illonite shows hydroxyl groups disposed mostly subparallel to the clay layer, which for each case influences the tight binding of anhydrous Na⁺ in the ditrigonal cavity (without any coordinating water molecules).

Two-dimensional density profiles of the surfaces indicate the stable nature of this minor adsorption site for the hectorite nanopore, while the diffuse distribution of Na⁺ in the next water layer is remarkably similar for both clay nanopores. A most striking difference between the two nanopores is observed in the surface density profiles for the two water layers at the clay surfaces. Water on hectorite exhibits a structure that mirrors the hexagonal symmetry of the siloxane surface, while montmorillonite displays an asymmetry to the density contours that most likely represents the vacancy in the octahedral sheet. This is a remarkable difference in water structure given that both clay minerals have the equivalent siloxane sheet exposed to the aqueous solution of the nanopore.

The large simulation cells (roughly 80 Å × 70 Å × 90 Å) and long simulation times (>50 ns) provide significant improvements in the statistics associated with MD trajectory analysis of interfacial behavior while reducing periodic boundary interactions for a larger representative surface and contributing to a better representation of long-range lateral interactions on that surface. Additionally, a detailed view of solution transport through the expanded interlayers (nanopores) is provided through a rigorous analysis of diffusional motion in each aqueous layer near the surface. As a result, the molecular simulations represent an improvement in the analysis of adsorption behavior and associated residence times, and in determining diffusion rates of cations and water as affected by the clay mineral surfaces.

AUTHOR INFORMATION

Corresponding Author

*E-mail: jagreat@sandia.gov.

Notes

The authors declare no competing financial interest.

ACKNOWLEDGMENTS

We would like to thank Christin Morrow for helpful discussions. This work is supported by the U.S. Department of Energy, Office of Science, Office of Basic Energy Sciences, Geosciences Research Program. Sandia National Laboratories is a multiprogram laboratory managed and operated by Sandia Corporation, a wholly owned subsidiary of Lockheed Martin Corporation, for the U.S. Department of Energy's National Nuclear Security Administration under Contract DE-AC04-94AL85000.

REFERENCES

- (1) Zachara, J. M.; Serne, J.; Freshley, M.; Mann, F.; Anderson, F.; Wood, M.; Jones, T.; Myers, D. Geochemical Processes Controlling Migration of Tank Wastes in Hanford's Vadose Zone. *Vadose Zone J.* **2007**, *6*, 985–1003.
- (2) Sposito, G.; Skipper, N. T.; Sutton, R.; Park, S. H.; Soper, A. K.; Greathouse, J. A. Surface Geochemistry of the Clay Minerals. *Proc. Natl. Acad. Sci. U.S.A.* **1999**, *96*, 3358–3364.
- (3) Javadpour, F.; Fisher, D.; Unsworth, M. Nanoscale Gas Flow in Shale Gas Sediments. *J. Can. Pet. Technol.* **2007**, *46*, 55–61.
- (4) Loucks, R. G.; Reed, R. M.; Ruppel, S. C.; Jarvie, D. M. Morphology, Genesis, and Distribution of Nanometer-Scale Pores in Siliceous Mudstones of the Mississippian Barnett Shale. *J. Sediment. Res.* **2009**, *79*, 848–861.

- (5) Ning, Z. F.; Wang, B.; Yang, F.; Zeng, Y.; Chen, J. E.; Zhang, L. Microscale Effect of Microvadoses in Shale Reservoirs. *Pet. Explor. Dev.* **2014**, *41*, 492–499.

- (6) Kaszuba, J. P.; Janecky, D. R.; Snow, M. G. Experimental Evaluation of Mixed Fluid Reactions between Supercritical Carbon Dioxide and NaCl Brine: Relevance to the Integrity of a Geologic Carbon Repository. *Chem. Geol.* **2005**, *217*, 277–293.

- (7) Shao, H.; Ray, J. R.; Jun, Y.-S. Dissolution and Precipitation of Clay Minerals under Geologic CO₂ Sequestration Conditions: CO₂-Brine-Phlogopite Interactions. *Environ. Sci. Technol.* **2010**, *44*, 5999–6005.

- (8) Cole, D. R.; Chialvo, A. A.; Rother, G.; Vlcek, L.; Cummings, P. T. Supercritical Fluid Behavior at Nanoscale Interfaces: Implications for CO₂ Sequestration in Geologic Formations. *Philos. Mag.* **2010**, *90*, 2339–2363.

- (9) Bowers, G. M.; Hoyt, D. W.; Burton, S. D.; Ferguson, B. O.; Varga, T.; Kirkpatrick, R. J. In Situ C-13 and Na-23 Magic Angle Spinning NMR Investigation of Supercritical CO₂ Incorporation in Smectite–Natural Organic Matter Composites. *J. Phys. Chem. C* **2014**, *118*, 3564–3573.

- (10) Bodvarsson, G. S.; Boyle, W.; Patterson, R.; Williams, D. Overview of Scientific Investigations at Yucca Mountain—The Potential Repository for High-Level Nuclear Waste. *J. Contam. Hydrol.* **1999**, *38*, 3–24.

- (11) Long, J. C. S.; Ewing, R. C. Yucca Mountain: Earth-Science Issues at a Geologic Repository for High-Level Nuclear Waste. *Annu. Rev. Earth Planet. Sci.* **2004**, *32*, 363–401.

- (12) Pusch, R. Clays and Nuclear Waste Management. In *Handbook of Clay Science*, Second ed.; Bergaya, F., Theng, B. K. G., Lagaly, G., Eds.; Elsevier: Amsterdam, 2006; Vol. 1, pp 703–716.

- (13) Sellin, P.; Leupin, O. X. The Use of Clay as an Engineered Barrier in Radioactive-Waste Management—A Review. *Clays Clay Miner.* **2013**, *61*, 477–498.

- (14) Davis, J. A.; Yabusaki, S. B.; Steefel, C. I.; Zachara, J. M.; Curtis, G. P.; Redden, G. D.; Criscenti, L. J.; Honeyman, B. D. Assessing Conceptual Models for Subsurface Reactive Transport of Inorganic Contaminants. *EOS* **2004**, *85*, 449–455.

- (15) Goldberg, S.; Criscenti, L. J.; Turner, D. R.; Davis, J. A.; Cantrell, K. J. Adsorption–Desorption Processes in Subsurface Reactive Transport Modeling. *Vadose Zone J.* **2007**, *6*, 407–435.

- (16) Rose, D. A.; Abbas, F.; Adey, M. A. The Effect of Surface–Solute Interactions on the Transport of Solutes through Porous Materials. *Eur. J. Soil Sci.* **2009**, *60*, 398–411.

- (17) Zhang, S.; Kent, D. B.; Elbert, D. C.; Shi, Z.; Davis, J. A.; Veblen, D. R. Mineralogy, Morphology, and Textural Relationships in Coatings on Quartz Grains in Sediments in a Quartz-Sand Aquifer. *J. Contam. Hydrol.* **2011**, *124*, 57–67.

- (18) Zhao, Q.; Burns, S. E. Modeling Sorption and Diffusion of Organic Sorbate in Hexadecyltrimethylammonium-Modified Clay Nanopores—A Molecular Dynamics Simulation Study. *Environ. Sci. Technol.* **2013**, *47*, 2769–2776.

- (19) Botan, A.; Rotenberg, B.; Marry, V.; Turq, P.; Noetinger, B. Hydrodynamics in Clay Nanopores. *J. Phys. Chem. C* **2011**, *115*, 16109–16115.

- (20) Botan, A.; Marry, V.; Rotenberg, B.; Turq, P.; Noetinger, B. How Electrostatics Influences Hydrodynamic Boundary Conditions: Poiseuille and Electro-Osmotic Flows in Clay Nanopores. *J. Phys. Chem. C* **2013**, *117*, 978–985.

- (21) Jaramillo-Botero, A.; Nielsen, R.; Abrol, R.; Su, J.; Pascal, T.; Mueller, J.; Goddard, W. A., III. First-Principles-Based Multiscale, Multiparadigm Molecular Mechanics and Dynamics Methods for Describing Complex Chemical Processes. In *Multiscale Molecular Methods in Applied Chemistry*; Kirchner, B., Vrabec, J., Eds.; Springer-Verlag: Berlin/Heidelberg, 2012; Vol. 307, pp 1–42.

- (22) Mehmani, Y.; Sun, T.; Balhoff, M. T.; Eichhubl, P.; Bryant, S. Multiblock Pore-Scale Modeling and Upscaling of Reactive Transport: Application to Carbon Sequestration. *Transp. Porous Media* **2012**, *95*, 305–326.

- (23) Xian, L.; Zeiml, M.; Lackner, R.; Mang, H. A. Upscaling of Permeability of Porous Materials: First Insight into the Effect of Pore-Space Characteristics. *Int. J. Multiscale Comput. Eng.* **2010**, *8*, 103–112.
- (24) Bourg, I. C.; Sposito, G. Connecting the Molecular Scale to the Continuum Scale for Diffusion Processes in Smectite-Rich Porous Media. *Environ. Sci. Technol.* **2010**, *44*, 2085–2091.
- (25) Porion, P.; Delville, A. Multinuclear NMR Study of the Structure and Micro-Dynamics of Counterions and Water Molecules within Clay Colloids. *Curr. Opin. Colloid Interface Sci.* **2009**, *14*, 216–222.
- (26) Bowers, G. M.; Bish, D. L.; Kirkpatrick, R. J. H₂O and Cation Structure and Dynamics in Expandable Clays: ²H and ³⁹K NMR Investigations of Hectorite. *J. Phys. Chem. C* **2008**, *112*, 6430–6438.
- (27) Bowers, G. M.; Singer, J. W.; Bish, D. L.; Kirkpatrick, R. J. Alkali Metal and H₂O Dynamics at the Smectite/Water Interface. *J. Phys. Chem. C* **2011**, *115*, 23395–23407.
- (28) Bowers, G. M.; Singer, J. W.; Bish, D. L.; Kirkpatrick, R. J. Structural and Dynamical Relationships of Ca²⁺ and H₂O in Smectite/H₂O Systems. *Am. Mineral.* **2014**, *99*, 318–331.
- (29) Ishimaru, S.; Ikeda, R. NMR Studies on Dynamics of Water Intercalated in Clay Minerals. *Z. Naturforsch., A* **1999**, *54*, 431–436.
- (30) Porion, P.; Delville, A. NMR Studies and Multi-Scale Modeling of the Water and Ionic Mobilities within the Porous Networks Limited by Clay Particles. *Ann. Chim.* **2005**, *30*, 263–276.
- (31) Porion, P.; Faugere, A. M.; Delville, A. Dynamical Properties of Ions Confined within Dense Dispersions of Charged Anisotropic Colloids: A Na-23 Quadrupolar NMR Study. *Eur. Phys. J.: Spec. Top.* **2007**, *141*, 281–284.
- (32) Tenorio, R. P.; Alme, L. R.; Engelsberg, M.; Fossum, J. O.; Hallwass, F. Geometry and Dynamics of Intercalated Water in Na-Fluorhectorite Clay Hydrates. *J. Phys. Chem. C* **2008**, *112*, 575–580.
- (33) Weiss, C. A.; Kirkpatrick, R. J.; Altaner, S. P. The Structural Environments of Cations Adsorbed onto Clays: ¹³³Cs Variable-Temperature MAS NMR Spectroscopic Study of Hectorite. *Geochim. Cosmochim. Acta* **1990**, *54*, 1655–1669.
- (34) Weiss, C. A.; Kirkpatrick, R. J.; Altaner, S. P. Variations in Interlayer Cation Sites as Studied by ¹³³Cs MAS Nuclear Magnetic Resonance Spectroscopy. *Am. Mineral.* **1990**, *75*, 970–982.
- (35) Morrow, C. P.; Yazaydin, A. Ö.; Krishnan, M.; Bowers, G. M.; Kalinichev, A. G.; Kirkpatrick, R. J. Structure, Energetics, and Dynamics of Smectite Clay Interlayer Hydration: Molecular Dynamics and Metadynamics Investigation of Na-Hectorite. *J. Phys. Chem. C* **2013**, *117*, 5172–5187.
- (36) Marry, V.; Dubois, E.; Malikova, N.; Durand-Vidal, S.; Longeville, S.; Breu, J. Water Dynamics in Hectorite Clays: Influence of Temperature Studied by Coupling Neutron Spin Echo and Molecular Dynamics. *Environ. Sci. Technol.* **2011**, *45*, 2850–2855.
- (37) Marry, V.; Dubois, E.; Malikova, N.; Breu, J.; Haussler, W. Anisotropy of Water Dynamics in Clays: Insights from Molecular Simulations for Experimental QENS Analysis. *J. Phys. Chem. C* **2013**, *117*, 15106–15115.
- (38) Malikova, N.; Cadene, A.; Marry, V.; Dubois, E.; Turq, P. Diffusion of Water in Clays on the Microscopic Scale: Modeling and Experiment. *J. Phys. Chem. B* **2006**, *110*, 3206–3214.
- (39) Malikova, N.; Dubois, E.; Marry, V.; Rotenberg, B.; Turq, P. Dynamics in Clays—Combining Neutron Scattering and Microscopic Simulation. *Z. Phys. Chem.* **2010**, *224*, 153–181.
- (40) Kosakowski, G.; Churakov, S. V.; Thoenen, T. Diffusion of Na and Cs in Montmorillonite. *Clays Clay Miner.* **2008**, *56*, 190–206.
- (41) Liu, X.; Lu, X.; Wang, R.; Zhou, H. Effects of Layer-Charge Distribution on the Thermodynamic and Microscopic Properties of Cs-Smectite. *Geochim. Cosmochim. Acta* **2008**, *72*, 1837–1847.
- (42) Malikova, N.; Marry, V.; Dufrière, J. F.; Simon, C.; Turq, P.; Giffaut, E. Temperature Effect in a Montmorillonite Clay at Low Hydration-Microscopic Simulation. *Mol. Phys.* **2004**, *102*, 1965–1977.
- (43) Marry, V.; Turq, P.; Cartailier, T.; Levesque, D. Microscopic Simulation of Structure and Dynamics of Water and Counterions in a Monohydrated Montmorillonite. *J. Chem. Phys.* **2002**, *117*, 3454–3463.
- (44) Marry, V.; Turq, P. Microscopic Simulations of Interlayer Structure and Dynamics in Bihydrated Heteroionic Montmorillonites. *J. Phys. Chem. B* **2003**, *107*, 1832–1839.
- (45) Sutton, R.; Sposito, G. Animated Molecular Dynamics Simulations of Hydrated Caesium-Smectite Interlayers. *Geochem. Trans.* **2002**, *3*, 73–80.
- (46) Rotenberg, B.; Marry, V.; Malikova, N.; Turq, P. Molecular Simulation of Aqueous Solutions at Clay Surfaces. *J. Phys.: Condens. Mater.* **2010**, *22*.
- (47) Wang, J.; Kalinichev, A. G.; Kirkpatrick, R. J. Molecular Modeling of Water Structure in Nano-Pores between Brucite (001) Surfaces. *Geochim. Cosmochim. Acta* **2004**, *68*, 3351–3365.
- (48) Criscenti, L. J.; Cygan, R. T.; Kooser, A. S.; Moffat, H. K. Water and Halide Adsorption to Corrosion Surfaces: Molecular Simulations of Atmospheric Interactions with Aluminum Oxyhydroxide and Gold. *Chem. Mater.* **2008**, *20*, 4682–4693.
- (49) Wang, J.; Kalinichev, A. G.; Kirkpatrick, R. J.; Cygan, R. T. Structure, Energetics, and Dynamics of Water Adsorbed on the Muscovite (001) Surface: A Molecular Dynamics Simulation. *J. Phys. Chem. B* **2005**, *109*, 15893–15905.
- (50) Bourg, I. C.; Sposito, G. Molecular Dynamics Simulations of the Electrical Double Layer on Smectite Surfaces Contacting Concentrated Mixed Electrolyte (NaCl–CaCl₂) Solutions. *J. Colloid Interface Sci.* **2011**, *360*, 701–715.
- (51) Holmboe, M.; Bourg, I. C. Molecular Dynamics Simulations of Water and Sodium Diffusion in Smectite Interlayer Nanopores as a Function of Pore Size and Temperature. *J. Phys. Chem. C* **2014**, *118*, 1001–1013.
- (52) Martins, D. M. S.; Molinari, M.; Goncalves, M. A.; Mirao, J. P.; Parker, S. C. Toward Modeling Clay Mineral Nanoparticles: The Edge Surfaces of Pyrophyllite and Their Interaction with Water. *J. Phys. Chem. C* **2014**, *118*, 27308–27317.
- (53) Wang, J. W.; Kalinichev, A. G.; Kirkpatrick, R. J. Effects of Substrate Structure and Composition on the Structure, Dynamics, and Energetics of Water at Mineral Surfaces: A Molecular Dynamics Modeling Study. *Geochim. Cosmochim. Acta* **2006**, *70*, 562–582.
- (54) Hartzell, C. J.; Cygan, R. T.; Nagy, K. L. Molecular Modeling of the Tributyl Phosphate Complex of Europium Nitrate in the Clay Hectorite. *J. Phys. Chem. A* **1998**, *102*, 6722–6729.
- (55) Cygan, R. T.; Liang, J.-J.; Kalinichev, A. G. Molecular Models of Hydroxide, Oxyhydroxide, and Clay Phases and the Development of a General Force Field. *J. Phys. Chem. B* **2004**, *108*, 1255–1266.
- (56) Wang, J.; Kalinichev, A. G.; Amonette, J. E.; Kirkpatrick, R. J. Interlayer Structure and Dynamics of Cl-Bearing Hydrotalcite: Far Infrared Spectroscopy and Molecular Dynamics Modeling. *Am. Mineral.* **2003**, *88*, 398–409.
- (57) Kumar, P. P.; Kalinichev, A. G.; Kirkpatrick, R. J. Hydration, Swelling, Interlayer Structure, and Hydrogen Bonding in Organolayered Double Hydroxides: Insights from Molecular Dynamics Simulation of Citrate-Intercalated Hydrotalcite. *J. Phys. Chem. B* **2006**, *110*, 3841–3844.
- (58) Liu, X. D.; Lu, X. C. A Thermodynamic Understanding of Clay-Swelling Inhibition by Potassium Ions. *Angew. Chem., Int. Ed.* **2006**, *45*, 6300–6303.
- (59) Ferrage, E.; Sakharov, B. A.; Michot, L. J.; Delville, A.; Bauer, A.; Lanson, B.; Grangeon, S.; Frapper, G.; Jimenez-Ruiz, M.; Cuellar, G. J. Hydration Properties and Interlayer Organization of Water and Ions in Synthetic Na-Smectite with Tetrahedral Layer Charge: Part 2. Toward a Precise Coupling between Molecular Simulations and Diffraction Data. *J. Phys. Chem. C* **2011**, *115*, 1867–1881.
- (60) Kalinichev, A. G.; Kirkpatrick, R. J. Molecular Dynamics Modeling of Chloride Binding to the Surfaces of Calcium Hydroxide, Hydrated Calcium Aluminate, and Calcium Silicate Phases. *Chem. Mater.* **2002**, *14*, 3539–3549.
- (61) Kerisit, S.; Liu, C. X.; Ilton, E. S. Molecular Dynamics Simulations of the Orthoclase (001)- and (010)-Water Interfaces. *Geochim. Cosmochim. Acta* **2008**, *72*, 1481–1497.

- (62) Cygan, R. T.; Greathouse, J. A.; Heinz, H.; Kalinichev, A. G. Molecular Models and Simulations of Layered Materials. *J. Mater. Chem.* **2009**, *19*, 2470–2481.
- (63) Wander, M. C. F.; Clark, A. E. Structural and Dielectric Properties of Quartz–Water Interfaces. *J. Phys. Chem. C* **2008**, *112*, 19986–19994.
- (64) Malani, A.; Ayappa, K. G. Adsorption Isotherms of Water on Mica: Redistribution and Film Growth. *J. Phys. Chem. B* **2009**, *113*, 1058–1067.
- (65) Argyris, D.; Ho, T. A.; Cole, D. R.; Striolo, A. Molecular Dynamics Studies of Interfacial Water at the Alumina Surface. *J. Phys. Chem. C* **2011**, *115*, 2038–2046.
- (66) Greathouse, J. A.; Cygan, R. T. Molecular Dynamics Simulation of Uranyl(VI) Adsorption Equilibria onto an External Montmorillonite Surface. *Phys. Chem. Chem. Phys.* **2005**, *7*, 3580–3586.
- (67) Greathouse, J. A.; Cygan, R. T. Water Structure and Aqueous Uranyl(VI) Adsorption Equilibria onto External Surfaces of Beidellite, Montmorillonite, and Pyrophyllite: Results from Molecular Simulations. *Environ. Sci. Technol.* **2006**, *40*, 3865–3871.
- (68) Vasconcelos, I. F.; Bunker, B. A.; Cygan, R. T. Molecular Dynamics Modeling of Ion Adsorption to the Basal Surfaces of Kaolinite. *J. Phys. Chem. C* **2007**, *111*, 6753–6762.
- (69) Hou, D. S.; Li, Z. J. Molecular Dynamics Study of Water and Ions Transport in Nano-Pore of Layered Structure: A Case Study of Tobermorite. *Microporous Mesoporous Mater.* **2014**, *195*, 9–20.
- (70) Plimpton, S. Fast Parallel Algorithms for Short-Range Molecular Dynamics. *J. Comput. Phys.* **1995**, *117*, 1–19.
- (71) Plimpton, S. J.; Pollock, R.; Stevens, M. J. *Particle-Mesh Ewald and rRESPA for Parallel Molecular Dynamics Simulations*; Proceedings of the Eighth SIAM Conference on Parallel Processing for Scientific Computing, Minneapolis, Minnesota, 1997.
- (72) Teich-McGoldrick, S. L.; Greathouse, J. A.; Cygan, R. T. Molecular Dynamics Simulations of Uranyl Adsorption and Structure on the Basal Surface of Muscovite. *Mol. Simul.* **2014**, *40*, 610–617.
- (73) Zeitler, T. R.; Greathouse, J. A.; Cygan, R. T. Effects of Thermodynamic Ensemble and Mineral Surface on Interfacial Water Structure. *Phys. Chem. Chem. Phys.* **2012**, *14*, 1728–1734.
- (74) Greathouse, J. A.; Hart, D. B.; Ochs, M. E. Alcohol and Thiol Adsorption on (Oxy)Hydroxide and Carbon Surfaces: Molecular Dynamics Simulation and Desorption Experiments. *J. Phys. Chem. C* **2012**, *116*, 26756–26764.
- (75) Liu, P.; Harder, E.; Berne, B. J. On the Calculation of Diffusion Coefficients in Confined Fluids and Interfaces with an Application to the Liquid–Vapor Interface of Water. *J. Phys. Chem. B* **2004**, *108*, 6595–6602.
- (76) Bergaya, F.; Lagaly, G. General Introduction: Clays, Clay Minerals, and Clay Science. In *Handbook of Clay Science*, second ed.; Bergaya, F., Lagaly, G., Eds.; Elsevier: Amsterdam, 2013; Vol. 5, pp 1–19.
- (77) Larentzos, J. P.; Greathouse, J. A.; Cygan, R. T. An Ab Initio and Classical Molecular Dynamics Investigation of the Structural and Vibrational Properties of Talc and Pyrophyllite. *J. Phys. Chem. C* **2007**, *111*, 12752–12759.
- (78) Billes, W.; Bazant-Hegemark, F.; Mecke, M.; Wendland, M.; Fischer, J. Change of Free Energy During Adsorption of a Molecule. *Langmuir* **2003**, *19*, 10862–10868.
- (79) Cao, F. L.; Sun, Y. X.; Wang, L.; Sun, H. Kinetic Effects in Predicting Adsorption Using the GCMC Method—Using CO₂ Adsorption on ZIFs As an Example. *RSC Adv.* **2014**, *4*, 27571–27581.
- (80) Katz, L. E.; Criscenti, L. J.; Chen, C. C.; Larentzos, J. P.; Liljestrand, H. M. Temperature Effects on Alkaline Earth Metal Ions Adsorption on Gibbsite: Approaches from Macroscopic Sorption Experiments and Molecular Dynamics Simulations. *J. Colloid Interface Sci.* **2013**, *399*, 68–76.
- (81) Joung, I. S.; Cheatham, T. E. Molecular Dynamics Simulations of the Dynamic and Energetic Properties of Alkali and Halide Ions Using Water-Model-Specific Ion Parameters. *J. Phys. Chem. B* **2009**, *113*, 13279–13290.
- (82) Koneshan, S.; Rasaiah, J. C.; Lynden-Bell, R. M.; Lee, S. H. Solvent Structure, Dynamics, and Ion Mobility in Aqueous Solutions at 25 °C. *J. Phys. Chem. B* **1998**, *102*, 4193–4204.
- (83) Marry, V.; Rotenberg, B.; Turq, P. Structure and Dynamics of Water at a Clay Surface from Molecular Dynamics Simulation. *Phys. Chem. Chem. Phys.* **2008**, *10*, 4802–4813.
- (84) Botan, A.; Marry, V.; Rotenberg, B. Diffusion in Bulk Liquids: Finite-Size Effects in Anisotropic Systems. *Mol. Phys.* **2015**, 1–6.